Chinese Journal of Mechanical Engineering

ORIGINAL ARTICLE

Open Access

# Theoretical and Experimental Study on the Performance of Hermetic Diaphragm Squeeze Film Dampers for Gas-Lubricated Bearings

Jianwei Wang[1], Haoxi Zhang[1], Shaocun Han[1], Hang Li[1], Peng Wang[1] and Kai Feng[1*]

**Abstract**

Low damping characteristics have always been a key sticking points in the development of gas bearings. The application of squeeze film dampers can significantly improve the damping performance of gas lubricated bearings. This paper proposed a novel hermetic diaphragm squeeze film damper (HDSFD) for oil-free turbomachinery supported by gas lubricated bearings. Several types of HDSFDs with symmetrical structure were proposed for good damping performance. By considering the compressibility of the damper fluid, based on hydraulic fluid mechanics theory, a dynamic model of HDSFDs under medium is proposed, which successfully reflects the frequency dependence of force coefficients. Based on the dynamic model, the effects of damper fluid viscosity, bulk modulus of damper fluid, thickness of damper fluid film and plunger thickness on the dynamic stiffness and damping of HDSFDs were analyzed. An experimental test rig was assembled and series of experimental studies on HDSFDs were conducted. The damper fluid transverse flow is added to the existing HDSFD concept, which aims to make the dynamic force coefficients independent of frequency. Although the force coefficient is still frequency dependent, the damping coefficient at high frequency excitation with damper fluid supply twice as that without damper fluid supply. The results serve as a benchmark for the calibration of analytical tools under development.

**Keywords** Hermetic diaphragm squeeze film damper, Compressibility, Dynamic model, Experimental studies

## 1 Introduction

Gas-lubricated bearings are becoming more and more widely used due to their advantages of low friction, no pollution, long life and high-power density, especially in the field of oil-free turbomachinery, such as turbo-compressor systems for fuel cells and heat pumps, generators for portable gas or air turbines, printed circuit board (PCB) drilling, and optical devices [1–5]. These applications have rotational speeds from $10^4$ r/min to $10^6$ r/min and power ratings in tens to thousands of kilowatts. However, poor dynamic stability caused by self-excited vibrations has become a major obstacle to the further development of gas bearings.

Improving the damping characteristics of gas lubricated bearings is the most effective way to enhance stability. Coupling appropriate dampers to gas-lubricated bearings is an important way to improve the damping characteristics of the bearings. Metal mesh damper (MMD) [6–10] and squeeze film damper (SFD) [11–14] are commonly used in turbomachinery. Zaccardo and Buckner [15] extended this work by building a finite element model and data optimization. Lee et al. [9] presented load capacity tests of a metal mesh foil bearing at different rotational speeds. Ertas [16] coupled metal

*Correspondence:
Kai Feng
jkai.feng@gmail.com
[1] State Key Laboratory of Advanced Design and Manufacturing for Vehicle Body, Hunan University, Changsha 410082, China

Springer Open

© The Author(s) 2024. **Open Access** This article is licensed under a Creative Commons Attribution 4.0 International License, which permits use, sharing, adaptation, distribution and reproduction in any medium or format, as long as you give appropriate credit to the original author(s) and the source, provide a link to the Creative Commons licence, and indicate if changes were made. The images or other third party material in this article are included in the article's Creative Commons licence, unless indicated otherwise in a credit line to the material. If material is not included in the article's Creative Commons licence and your intended use is not permitted by statutory regulation or exceeds the permitted use, you will need to obtain permission directly from the copyright holder. To view a copy of this licence, visit http://creativecommons.org/licenses/by/4.0/.

mesh dampers (MMDs) in a new compliant hybrid gas journal bearing and conducted experimental studies of the effect of MMDs on bearing stability and load carrying capacity. Feng et al. [17] proposed a systematic study of MMDs and their effect on the static and dynamic characteristics of flexure pivot tilting pad gas bearings (FPTPBs). The effects of many parameters on the static and dynamic characteristics of FPTPBs are discussed, damper mesh density, MMD radial interference are included. However, the equivalent damping produced by MMDs is far below the damping requirements of high-power turbomachinery (MW power class) [18].

The original open flow SFDs is considered to be an oil film journal bearing with a nonrotating journal, which consists basically of a thin oil film between two nonrotating members, the damper ring and the bearing housing. Della Pietra and Adiletta [19, 20] provided a comprehensive review of analytical and experimental works about SFDs. In their earlier works, the continuity equation and the Reynolds equation have been used to obtain the pressure field of journal bearings and SFDs, which provides accurate results in the low-speed range. Although open-flow SFDs have been well studied, they are clearly not suitable for oil-free turbomachinery due to the high potential for contamination of the surrounding environment [21–23]. To overcome the disadvantages of the open-flow SFDs, Ertas and Delgado [24, 25] proposed a novel hermetic-SFD (HSFD) with an integral plunger submersed in damper fluid. The new concept was shown to have a damping comparable to open-flow SFD at lower frequencies, while with smaller damping at higher frequencies. This means that the damper exhibits a significant frequency dependence, and they attribute this to cavitation and the asymmetry of the damper cavities. The authors make engineering design modifications then to the existing HSFD concept, aiming to make the dynamic coefficients frequency independent [25]. However, the final experimental results still show a significant frequency dependence, and the authors tried to attribute the cause of the frequency dependence to the flexible structure (diaphragms) this time. It does not seem entirely accurate to attribute the frequency dependence of HSFD exclusively to structural flexibility, considering that the cavities of the dampers presented in Ref. [25] are still not perfectly symmetrical (because the cavities have the same fillet angle and different radius).

The objective of this work is to develop a new compact optimized HDSFD with a symmetrical structure that can eventually be integrated into a flexible gas bearing system and operate in an oil-free environment. Several HDSFDs structures with symmetrical structure were proposed for good damping performance. In addition, a dynamic model of HDSFD is proposed based on the hydrodynamic theory while considering the variation of silicone oil bulk modulus under small displacement conditions. Based on the dynamic model, the effects of damper fluid viscosity, bulk modulus of dynamic model, thickness of damper fluid film and plunger thickness on the dynamic stiffness and damping of HDSFD were analyzed. The theoretical results provide guidance for the determination of the HDSFDs size. An experimental test rig was assembled and series of experimental studies on HDSFDs were conducted. The experimental results verify the correctness of the theoretical analysis. In addition, the damper fluid transverse flow is added to the existing HDSFD concept, which aims to make the dynamic force coefficients independent of frequency.

## 2 Structural Design and Evolution of HDSFD

Figure 1 presents the basic structure and evolution of HDSFDs. From Figure 1(a), it is noted that configuration-I HDSFD mainly consists of four components, namely

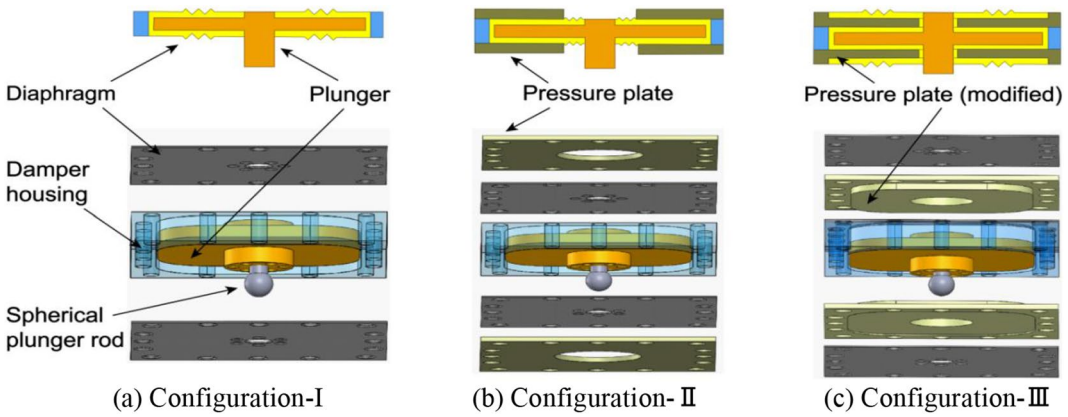


**Figure 1** Basic structure and evolution of HDSFDs

damper housing, plunger, spherical plunger rod and two flexible diaphragms. Flexible diaphragms made of spring steel are bolted to the housing and plunger respectively, and the contact surfaces of the different parts are sealed by gaskets. The cavity is formed between the two elastic diaphragms and the housing, and the cavity is filled with damper fluid. The plunger is completely submerged in the damper fluid and divides the cavity into two parts, the upper cavity and the lower one. The damper fluid between the upper and lower cavities is connected through the gap between the plunger and the damper housing. The external excitation drives the plunger through the plunger rod to vibrate inside the cavity, causing the volume of the upper and lower cavities to change, which in turn causes the damper fluid to flow between the upper and lower cavities. The damper fluid in the cavities is squeezed by the plunger to produce a reaction force that prevents the plunger from vibrating.

The elasticity of the diaphragms makes it sufficient to meet the flexibility requirements of the damper. However, the isotropic motion of the diaphragm and the plunger greatly weakens the squeezing effect of the plunger on the damper fluid, which is detrimental to the damping performance of the HDSFD. In order to overcome the damage to the damping performance of the HDSFD caused by the same directional motion of the diaphragm and the plunger, the structure of HDSFD is optimized as configuration-II. The main improvement of configuration-II over configuration-I is the addition of a pair of metal pressure plates with a thickness of 2 mm on the outside of the diaphragms, as shown in Figure 1(b). The external profile of the pressure plate is the same as the diaphragm. The center of the pressure plate is machined with a hole for damper assembly, and the presence of the reserved hole also leaves room for the elastic deformation of the diaphragm.

The presence of the pressure plate significantly improves the squeezing effect of the damper fluid in the cavity. But this change has a significant impact on the overall structural stiffness of the damper. To eliminate the adverse effect caused by the pressure plate, the pressure plate was modified in shape and placed inside the diaphragm, as shown in Figure 1(c). One side of the pressure plate is designed with a 1 mm deep groove for filling with damper fluid. Compared to configuration-I and configuration-II, configuration-III HDSFD has four layers of damper fluid film. The presence of the damper fluid film between the pressure plate (modified) and the elastic diaphragm plays a complementary role in the damping performance of configuration-III HDSFD. In addition, the two oil films in the interval position are always in the same state of stress (squeezed or not squeezed). The hole in the center of the pressure plate is designed to form a clearance fit with the cylindrical surface of the plunger, which provides an additional slit damping effect compared to configuration-II. The proposed configuration-III HDSFD has considerable benefits:

(1) Completely sealed structure without leakage. Due to the use of diaphragm-box structure, the relative movements of the plunger and the housing (fixed parts) is completely wrapped inside the damper, which can prevent air from penetrating into the damper, as well as the extravasation of the damper fluid.
(2) Large damping characteristics. The multi-layer structure of configuration-III HDSFD can be regarded as dampers arranged in parallel, which is obvious for the improvement of damping. What needs to be emphasized is the "face" damper concept and symmetrical structure of configuration-III HDSFD, both of which are useful for the optimization of the damping performance.

In addition to the improvements mentioned above, the effect of the external supply of damper fluid on the force coefficients of HDSFD is investigated based on configuration-II. Inlet and outlet nozzles are installed on the side of the damper housing of configuration-II. The damper fluid flows into the squeezing surface land through the inlet nozzles and flows out from the outlet subsequently, leaving the cavity filled with flowing damper fluid. This structure draws on the features of ISFD, as shown in Figure 2. The HDSFD with damper fluid supply version (configuration-IV) and one of its possible applications for high power oil-free turbomachinery is presented in Figure 2(b). An ISFD is also presented in Figure 2(a) as a comparison. The purpose of this exploration is to reduce the frequency dependence of HDSFD, considering the reality that the frequency dependence of ISFD is very small. The difference of them is that the damper fluid supplied to ISFD is drained directly, which tends to cause surrounding contamination, while the damper fluid in configuration-IV flows out through a set of pipelines, which keeps the damper fluid isolated from the outside world completely and allows for collection and circulation.

## 3 Dynamic Model of HDSFDs

There is no doubt that the performance of a fluidic viscous damper is influenced by a combination of structure, size, damper fluid properties and operating conditions. Among the many properties of damper fluid, compressibility is one of the important reasons for the frequency dependence, which is affected by a combination of operating conditions, air content, pressure, etc. [27–29].

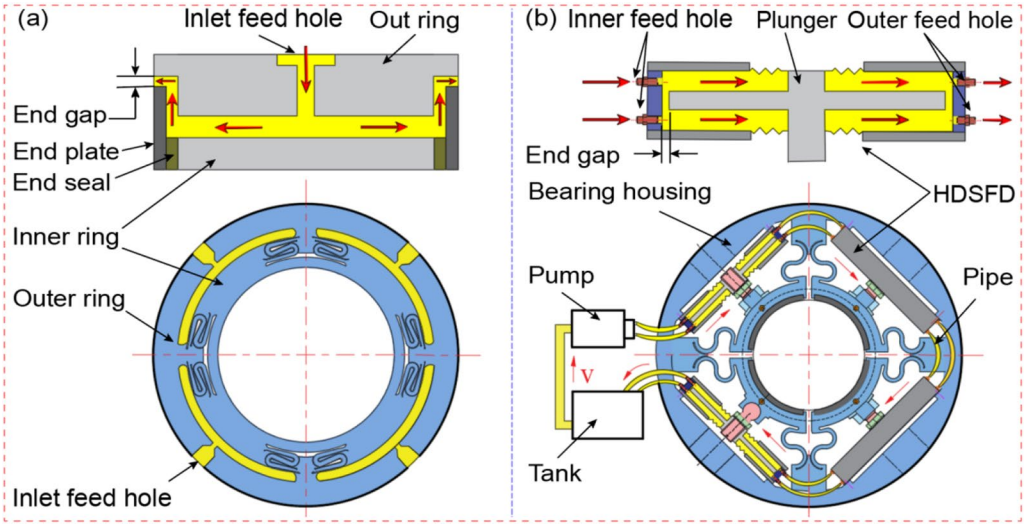


**Figure 2** Example of the application of SFD in gas bearings: **a** Cross-sectional view of the lubricant flow path of ISFD and schematic diagram of ISFD with S-spring [26], **b** Cross-sectional view of the lubricant flow path of HDSFD with damper fluid supply and one of possible applications

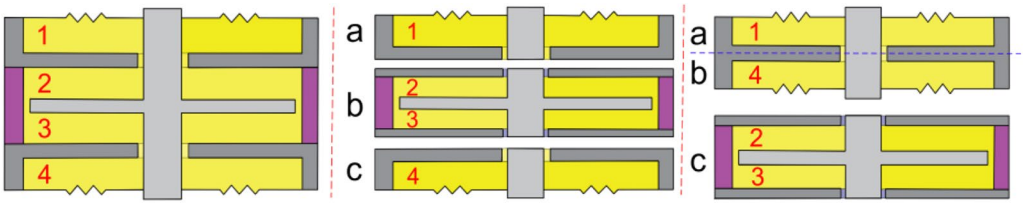


**Figure 3** Schematic of the configuration-III HDSFD

The configuration-III HDSFD contains four layers damper fluid films inside, two of which arranged at intervals (1, 3 or 2, 4) will be subjected to pressure in the same direction. The force acting on the plunger by the squeezed damper fluid can be divided into two parts. The one part originates from segment-b, which acts directly on the plunger like configuration-II, and the other part originates from segment-a and c, which is transmitted to the plunger through the diaphragms. Considering the symmetry of the segment-a and c, they are analyzed together, and segment-b is analyzed separately, as shown in Figure 3.

The schematic of different segments of configuration-III and the forces acting on the plunger as shown in Figure 4. The forces applied to the plunger by the combination of segment-a and c of configuration-III are similar to those of the plunger of segment-b. It should be noted that the schematic diagram of configuration-I and configuration-II and the forces applied to the plunger by damper fluid are the same as segment-b, due to the similarity in structure. The following work takes configuration-II as the object of study, based on the theory of hydraulic fluid dynamics, considering the

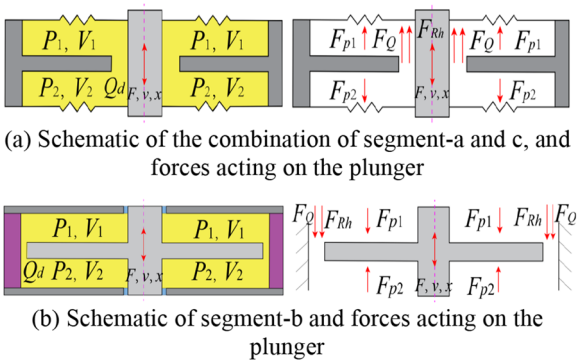


(a) Schematic of the combination of segment-a and c, and forces acting on the plunger

(b) Schematic of segment-b and forces acting on the plunger

**Figure 4** Schematic of different segments of HDSFD and the forces acting on the plunger

compressibility of the damper fluid, and establishes the dynamics model of the damper.

When the damper fluid flows in the cavity, a portion of the fluid passes through the slit from one side of the cavity to the other, while the rest of the fluid is compressed. According to the principle of flux conservation [29]:

$$\begin{cases} -Q_d + A_p v = V_1 \dot{P}_1 / \beta, \\ -Q_d - A_p v = V_2 \dot{P}_2 / \beta, \end{cases} \tag{1}$$

where, $Q_d$ is the flow rate through the slit. $A_p$ is the effective area of the plunger. $v$ is the permeability of porous materials. $V_1$ and $V_2$ denote the volume of the left- and right-side cavities, respectively. $P_1$ and $P_2$ are the pressures of the two cavities. $\beta$ represents the bulk modulus of the damper fluid.

Consider the flow of damper fluid in the slit as laminar flow, the equilibrium equation of the damper fluid in the gap can be written as:

$$F_{p1} - F_{p2} = F_{Rh} + F_Q, \tag{2}$$

where, $F_{P1}$ and $F_{P2}$ are the forces exerted by the damper fluid on the plunger. $F_{Rh}$ is the force produced by the resistance in the slit. $F_Q$ is the inertia force of the damper fluid in the slit. The forces presented above can be expressed as:

$$\begin{cases} F_{pi} = P_i A_g (i = 1, 2), \\ F_{Rh} = R_h Q_d A_g, \\ F_Q = \rho L_g \dot{Q}_d, \end{cases} \tag{3}$$

where, $A_g$ is the cross-sectional area of the slit. $\rho$ is the density of the damper fluid. $L_g$ is the thickness of the plunger. $R_h$ is defined as the ratio of small increments of differential pressure to small increments of flow at both ends of the slit.

$$R_h = \frac{\mathrm{d}P}{\mathrm{d}Q_d}. \tag{4}$$

The flow exchange between the two cavities can be expressed as:

$$Q_d = \frac{bh^3 \Delta P}{12 \mu L}. \tag{5}$$

Express the damping force as the pressure difference between the two cavities:

$$F = (P_1 - P_2) \cdot A_p. \tag{6}$$

Integrating the above equations yields the state equation of the system:

$$\dot{X} = AX + Bv, \tag{7}$$

$$A = \begin{bmatrix} 0 & 0 & -\beta / V_1 \\ 0 & 0 & \beta / V_1 \\ A_g / (\rho L_g) & -A_g / (\rho L_g) & -R_h A_g / (\rho L_g) \end{bmatrix},$$

$$B = \begin{bmatrix} \beta A_p / V_1 \\ -\beta A_p / V_2 \\ 0 \end{bmatrix}.$$

Considering that the excitation amplitude is much smaller than the damper fluid film thickness, it can be assumed that the cavity volume remains constant: $V_1 = V_2 = V_0$.

The transfer function can be expressed as:

$$G(s) = \frac{F(s)}{v(s)} = \frac{2\beta A_p^2 \left(s + \frac{R_h A_g}{\rho L_g}\right)}{v_0 \left(s^2 + R_h \frac{A_g}{\rho L_g} s + 2 \frac{A_g \beta}{\rho L_g v_0}\right)}. \tag{8}$$

When the plunger is disturbed by a small displacement, it can be described as $x = x_0 \sin \omega t$.

And

$$v = \dot{x}, \ v(s) = sX(s). \tag{9}$$

From Eq. (8) and Eq. (9), we have:

$$\frac{F(s)}{X(s)} = \frac{sG(s)}{v(s)} = \frac{2\beta A_p^2 s \left(s + \frac{R_h A_g}{\rho L_g}\right)}{v_0 \left(s^2 + R_h \frac{A_g}{\rho L_g} s + 2 \frac{A_g}{\rho L_g} \frac{\beta}{v_0}\right)}. \tag{10}$$

Eq. (10) can be deformed as:

$$\frac{F(s)}{X(s)} = K_0 \frac{s^2 + A_1 s}{s^2 + A_2 s + A_3}, \tag{11}$$

where

$K_0 = \frac{2\beta A_p^2}{V_0}, A_1 = A_2 = \frac{R_h A_g}{\rho L_g}, A_3 = \frac{2\beta A_g}{(\rho L_g) V_0}$.

From denominator of Eq. (11), it can be seen that the characteristic root is related to $R_h$, $A_g$, $L_g$, $\rho$, $\beta$, $V$. If the values of these parameters are changed, the pressure gradient force of the damper will be different. Thus, it is essential to analyze the distribution of the characteristic roots.

The discriminant of roots can be expressed as:

$$\Delta = A_2^2 - 4A_3 = \left(\frac{R_h A_g}{\rho L_g}\right)^2 - \frac{8\beta A_g}{(\rho L_g) V_0}. \tag{12}$$

(1) When $\Delta < 0$, the transfer function has a pair of conjugate complex roots, and the conjugate complex roots can be shown as:

$$s_1 = a + bj, s_2 = a - bj,$$

where

$$a = -\frac{A_2}{2}, b = \frac{\sqrt{|A_2^2 - 4A_3|}}{2}.$$

Eq. (11) can be rewritten as:

$$\frac{F(s)}{X(s)} = K_0 \frac{s^2 + A_1 s}{(s - s_1)(s - s_2)}. \tag{13}$$

For sinusoidal displacement excitation, it can be described as:

$$X(s) = \frac{x_0 \omega}{s^2 + \omega^2}. \tag{14}$$

By substituting Eq. (14) into Eq. (13) and performing the inverse Laplace transform, the time response of the pressure gradient can be obtained.

$$\begin{aligned} F(t) = K_0 x_0 \omega [&2U \cos \omega t - 2V \sin \omega t \\ &+ 2e^{at}(M_s \cos bt) - N_s \sin bt], \end{aligned} \tag{15}$$

$$K_0 = \frac{2\beta A_p^2}{V_0}, A_1 = A_2 = \frac{R_h A_g}{\rho L_g}, A_3 = \frac{2\beta A_g}{(\rho L_g) V_0}.$$

(2) When $\Delta > 0$, there are two different real roots for the transfer function, which can be shown as:

$$s_1 = -\frac{A_2}{2} + \frac{\sqrt{A_2^2 - 4A_3}}{2}, s_2 = -\frac{A_2}{2} - \frac{\sqrt{A_2^2 - 4A_3}}{2}.$$

The transfer function can be described as:

$$\frac{F(s)}{X(s)} = K_0 \frac{s^2 + A_1 s}{(s - s_1)(s - s_2)}. \tag{16}$$

Using the inverse Laplace transform, the time response of the pressure gradient force can be expressed as:

$$F(t) = K_0 x_0 \omega \left[2U \cos \omega t - 2V \sin \omega t + c_1 e^{s_1 t} + c_2 e^{s_2 t}\right]. \tag{17}$$

(3) When $\Delta = 0$, the two real roots are the same. They can be written as:

$$s_1 = s_2 = -\frac{A_2}{2}, \quad n = -\frac{A_2}{2}.$$

The transfer function is the same as Eq. (16). The time response of the pressure gradient force can be obtained by inverse Laplace transform.

$$F(t) = K_0 x_0 \omega \left[2U \cos \omega t - 2V \sin \omega t + (c_1 t + c_2) e^{nt}\right]. \tag{18}$$

The time domain expression for the differential pressure force can be expressed as:

$$\begin{cases} F(t) = F_p(t) + F_q(t), \\ F_p(t) = K_0 x_0 \omega (2U \cos \omega t - 2V \sin \omega t), \\ F_q(t) = K_0 x_0 \omega \left[2e^{at}(M_s \cos bt - N_s \sin \omega t)\right], \Delta < 0, \\ F_q(t) = K_0 x_0 \omega \left(c_1 e^{s_1 t} + c_2 e^{s_2 t}\right), \Delta > 0, \\ F_q(t) = K_0 x_0 \omega (c_1 t + c_2) e^{nt}, \Delta = 0, \end{cases} \tag{19}$$

where $F_p(t)$ is the steady-state component of the differential pressure force, including the elastic and damping forces. $F_q(t)$ is the transient component of the differential pressure force.

It can be seen that the transient component $F_q(t)$ decays exponentially at all times, and the transient component is negligible as time grows. The external displacement excitation can be expressed as:

$$x = x_0 \sin \omega t, \dot{x} = \omega x_0 \cos \omega t.$$

The steady-state component of the differential pressure force can be rewritten as:

$$F_p(t) = -2VK_0 x + 2UK_0 \dot{x}. \tag{20}$$

Due to the similarity of the forces on the plunger between structure-b and the combination of structure-a and structure-c, the steady-state component of the differential pressure force of the combination of structure-a and structure-c can be approximated as:

$$F_{pc}(t) = \lambda \cdot (-2VK_0 x + 2UK_0 \dot{x}), \tag{21}$$

where $\lambda$ is the influence coefficient of the flexible structure, which is related to the thickness and the material of the diaphragms, obtained by comparing the experimental value with the theoretical predicted value.

The steady-state component of the differential pressure force of HDSFD can be rewritten as:

$$F_{pM}(t) = (1 + \lambda) \cdot (-2VK_0 x + 2UK_0 \dot{x}). \tag{22}$$

From Eq. (22), the stiffness coefficient $K$ and damping coefficient $C$ of HDSFD can be expressed as:

$$\begin{aligned} K &= -2(1 + \lambda) \cdot VK_0 \omega, \\ C &= 2(1 + \lambda) \cdot UK_0. \end{aligned} \tag{23}$$

When $\Delta < 0$,

$$\begin{aligned} U &= \frac{A_2 A_3}{2\left[A_2^2 \omega^2 + \left(A_3 - \omega^2\right)\right]}, \\ V &= \frac{-\omega\left(A_2^2 + \omega^2 - A_3\right)}{2\left[A_2^2 \omega^2 + \left(A_3 - \omega^2\right)\right]}. \end{aligned} \tag{24}$$

Substituting Eq. (24) into Eq. (23), stiffness coefficient $K$ and damping coefficient $C$ of HDSFD can be expressed as:

$$K = \frac{\frac{2\beta A_p^2\omega^2(1+\lambda)}{V_0}\left[\left(\frac{12\mu A_g}{\rho bh^3}\right)^2+\omega^2-\frac{2\beta A_g}{\rho L_g V_0}\right]}{\left(\frac{12\mu A_g}{\rho bh^3}\right)^2\omega^2+\left(\frac{2\beta A_g}{\rho L_g V_0}-\omega^2\right)^2},$$
$$C = \frac{48\mu\beta^2 A_p^2 A_g^2(1+\lambda)}{\rho^2 bh^3 L_g V_2^2\left[\left(\frac{12\mu A_g}{\rho bh^3}\right)^2\omega^2+\left(\frac{2\beta A_g}{\rho L_g V_0}-\omega^2\right)^2\right]}. \quad (25)$$

When $\Delta > 0$,

$$U = \frac{A_2 A_3}{2\left[A_2^2\omega^2+(A_3-\omega^2)\right]},$$
$$V = \frac{-\omega\left(A_2^2+\omega^2-A_3\right)}{2\left[A_2^2\omega^2+(A_3-\omega^2)\right]}. \quad (26)$$

The results for the stiffness and damping coefficients are the same as Eq. (25).

When $\Delta = 0$, that is to say $A_2^2 - 4A_3 = 0$,

$$U = \frac{A_2^2}{8\left[A_2^2\omega^2+\left(\frac{A_2^2}{4}-\omega^2\right)^2\right]},$$
$$V = \frac{-\omega\left(3A_2^2+4\omega^2\right)}{8\left[A_2^2\omega^2+\left(\frac{A_2^2}{4}-\omega^2\right)^2\right]}. \quad (27)$$

Substituting Eq. (27) into Eq. (22), stiffness coefficient $K$ and damping coefficient $C$ of HDSFD can be expressed as:

$$K = \frac{\frac{\beta A_p^2\omega^2}{2V_0}(1+\lambda)\left[3\left(\frac{12\mu A_g}{\rho bh^3}\right)^2+4\omega^2\right]}{\left(\frac{12\mu A_g}{\rho bh^3}\right)^2\omega^2+\left(\frac{2\beta A_g}{\rho L_g V_0}-\omega^2\right)^2}, \quad (28)$$

$$C = \frac{\frac{\beta A_p^2}{2V_0}(1+\lambda)\left(\frac{12\mu A_g}{\rho bh^3}\right)^2}{\left[\left(\frac{12\mu A_g}{\rho bh^3}\right)^2\omega^2+\left(\frac{2\beta A_g}{\rho L_g V_0}-\omega^2\right)^2\right]}. \quad (29)$$

Considering the similarity between configuration-I, configuration-II and configuration-III HDSFD (they are even simpler than configuration-III), configuration-I and configuration-II are not analyzed separately.

## 4 Experimental Methods

A detailed description of the HDSFD installed on the test rig and components of the damper is illustrated in Figure 5. As shown in Figure 5(a), the test rig comprises a test article mounted on the fixing device rigidly and an electro-hydraulic exciter attached to the damper plunger. The plunger vibrates at high frequencies in the damper fluid under the drive of electro-hydraulic exciter to produce damping force. Compared to Figure 5(a), the supply (pump) and stabilization device (pulse damper and backpressure valve) of damper fluid is added in Figure 5(b), in order to study the effect of the damper fluid supply on the damping performance. Figure 5(c) presents a diagram of the main parts of HDSFD. Figure 5(d) presents an assembled HDSFD used to study the effect of oil supply on damping performance. The effects of different damper structures, diaphragm thicknesses, amplitudes, damper fluid viscosities and damper fluid flow rates on the performance of the dampers were investigated experimentally. General damper dimensions, description of the fluid properties, and test parameters are shown in Table 1.

Considering the vibration of the plunger as a single degree of freedom motion, the equation of motion of the plunger can be expressed as:

$$m\ddot{x}(t) + c\dot{x}(t) + kx(t) = f(t). \quad (30)$$

The plural form of plunger vibration can be expressed as:

$$x(t) = Xe^{i\omega t}, f(t) = Fe^{i\omega t}, \quad (31)$$

where $\omega$ indicates the excitation frequency of the electro-hydraulic exciter, and $i = \sqrt{-1}$.

Substituting Eq. (30) and Eq. (31) into Eq. (32) leads to the frequency domain expression for the equation of motion:

$$mA + i\omega Xc + kX = F. \quad (32)$$

The controlled movement applied to the plunger $X$ and the force response $F$ obtained from the pressure detector represent the discrete Fourier transform of the time varying signals. The effective force is obtained by subtracting the inertial force from the total force.

$$F_{eff} = F - mA = kX + i\omega Xc. \quad (33)$$

The dynamic impedance coefficient of the damper is obtained by dividing both sides Eq. (32) by the response $X$. The real part of the impedance coefficient stands for the dynamic stiffness and the imaginary part divided

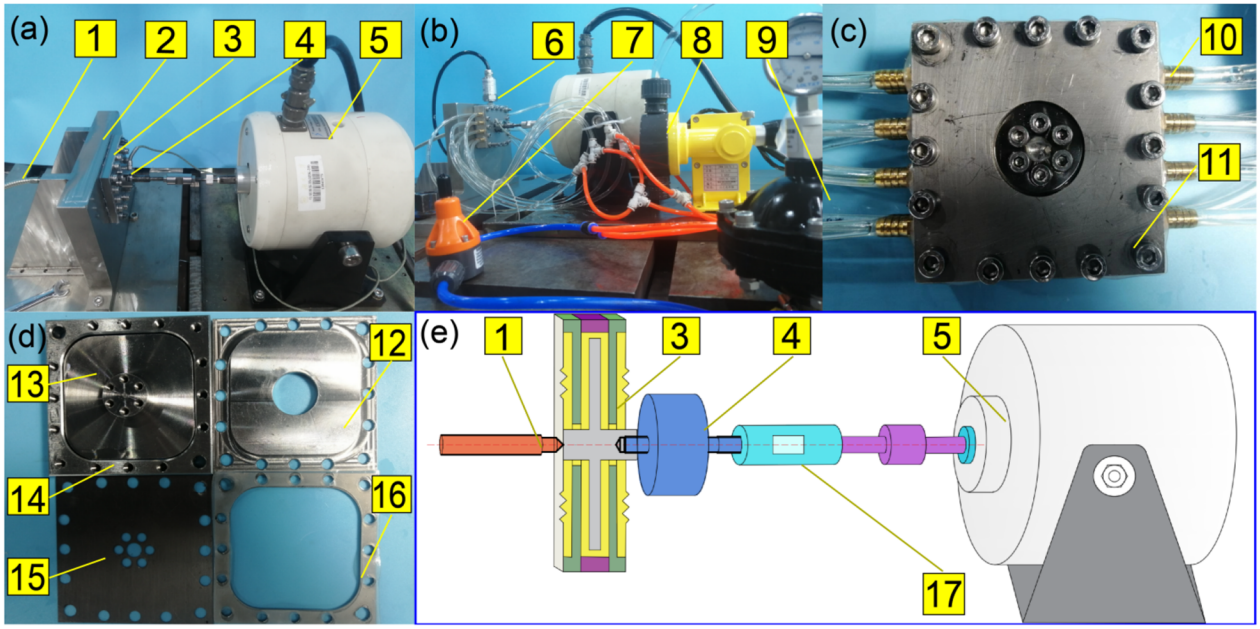


(1) Motion sensor, (2) Fixing device, (3) HDSFD, (4) Static/dynamic force cell, (5) Electro-hydraulic exciter, (6) Pressure transducer, (7) Backpressure valve, (8) Pump, (9) Pulse damper, (10) Inlet /outlet nozzles, (11) Pressure plate, (12) Pressure plate (modified), (13) Plunger, (14) Housing, (15) Diaphragms, (16) Shims, (17) Adjusting nut

**Figure 5** Test rig and arts composition of HDSFDs

**Table 1** Main parameters of HDSFD

| Parameters | Configuration-I HDSFD | Configuration-II HDSFD | Configuration-III HDSFD | Configuration-IV HDSFD | Unite |
|---|---|---|---|---|---|
| Plunger outline size of HDSFD | 5×64×65 | 5×64×65 | 5×64×65 | 5×64×65 | mm |
| Projected area | 36 | 36 | 36 | 36 | $cm^2$ |
| Film thickness $h$ | 1.5 | 1.5 | 1.5 | 2.5 | mm |
| End gap $h_v$ | 200 | 200 | 200 | 200 | μm |
| Damper fluid | Methyl silicone oil | Methyl silicone oil | Methyl silicone oil | Methyl silicone oil | – |
| Viscosity of damper fluid | 500, 1000, 1500 | 500, 1000, 1500 | 500, 1000, 1500 | 500, 1000, 1500 | $mm^2/s$ |
| Diaphragm thickness | 0.1, 0.3, 0.5 | 0.1, 0.3, 0.5 | 0.1, 0.3, 0.5 | 0.1, 0.3, 0.5 | mm |
| Diaphragm material | 304 stainless steel | 304 stainless steel | 304 stainless steel | 304 stainless steel | – |

by the excitation frequency obtains the damping coefficient.

$$H(\omega) = \frac{F_{eff}}{X} = k + ic\omega, \tag{33}$$

$$\mathrm{Re}(H) = k, \mathrm{Im}(H) = c\omega. \tag{34}$$

## 5 Results and Discussion

Figure 6 shows the predicted stiffness and damping coefficients of HDSFD versus different excitation frequencies with different squeeze film thicknesses. The viscosity of the damper fluid is 500 $mm^2/s$. The bulk modulus is 5.0 MPa and the plunger area is 36 $cm^2$. When $\lambda = 0$, it means that the diaphragm is perfectly flexible, its stiffness is zero-norm, and segment-a and c of configuration-III do not generate damping forces. As shown in Figure 6(a), when the excitation frequencies is less than 60 Hz, the stiffness coefficients increases rapidly at all squeeze film thicknesses. Nevertheless, when the excitation frequencies are higher than 60 Hz, the stiffness coefficients are found to have significant difference as the excitation frequencies increase with various squeeze film thicknesses. The predicted stiffness coefficients of the HDSFD with 1.5 mm film thickness are smaller than that of the HDSFD with 1.0 mm but always larger than

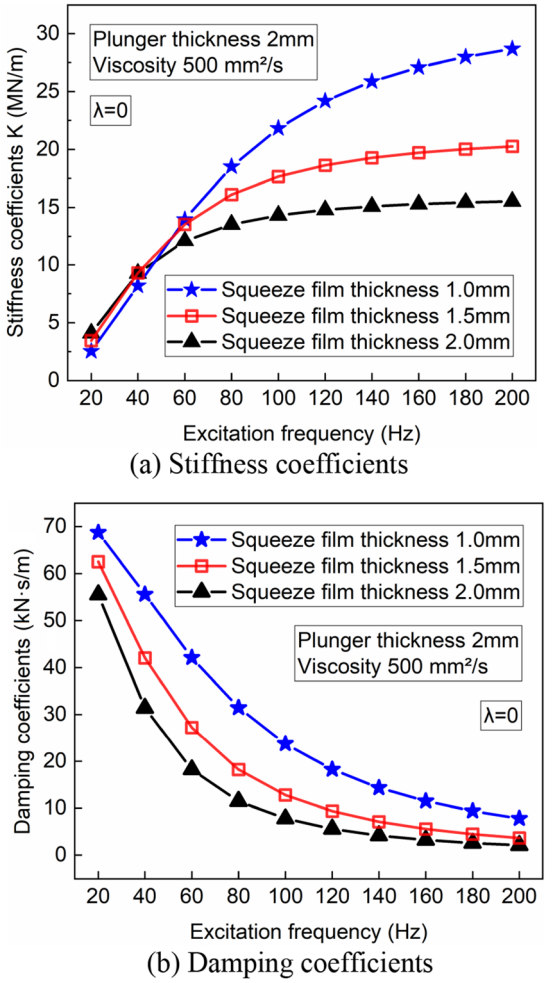


**Figure 6** Prediction of force coefficients for different squeeze film thicknesses

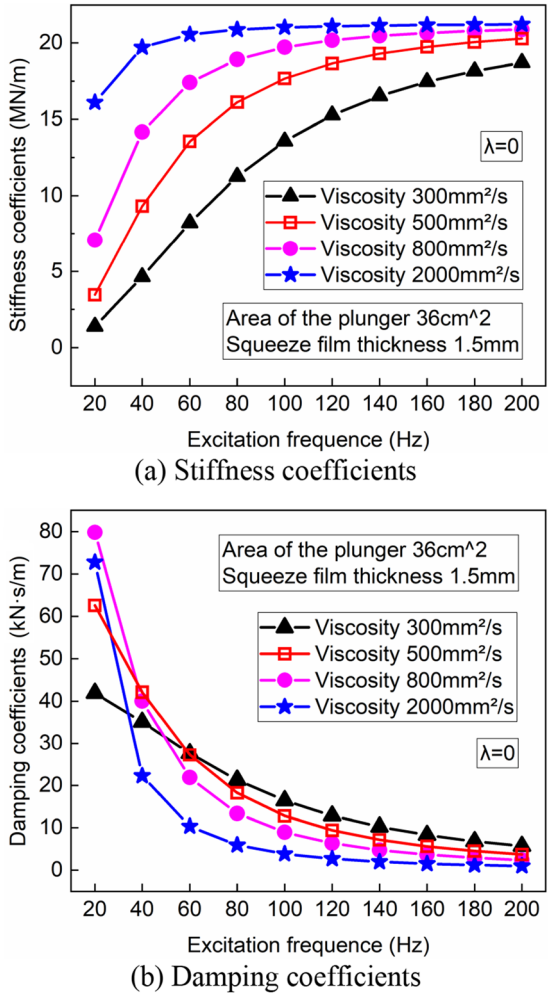


**Figure 7** Prediction of force coefficients for different damper fluid viscosities

that with 2.0 mm film thickness. As shown in Figure 6(b), the predicted damping coefficients of the HDSFD decrease with excitation frequencies, but the deceleration rate of that keep decreases with frequency. In addition, larger squeeze film thickness leads to lower damping coefficients.

Figure 7 illustrates the predicted stiffness and damping coefficients of HDSFD versus the viscosity of the damper fluid. As presented in Figure 7(a), the stiffness coefficients increase with the excitation frequency, but the growth rate of that keep decreases with frequency. In addition, the stiffness coefficient gradually increases with the viscosity of damper fluid. From Figure 7(b), it can be seen that the damping coefficient decreases with the increase of excitation frequency, and the deceleration rate of that keep decreases with excitation frequency. The maximum value of the damping coefficients increases first and then decreases with different viscosity of damper fluid. Damping coefficients decrease with the increase of viscosity when the excitation frequency is larger than 60 Hz. The damping coefficient of high-viscosity damper fluid decreases more rapidly with increasing excitation frequency than that of low-viscosity damper fluid. In other words, the HDSFD with high-viscosity damper fluids shows more obvious frequency dependence than that using low-viscosity damper fluids.

Figure 8 depicts the predicted stiffness and damping coefficients of HDSFD versus bulk modulus of the damper fluid at different excitation frequencies. It can be seen from Figure 8(a) that the stiffness coefficients increase with excitation frequency, while the growth rate of that keep decreases with frequency. The stiffness coefficients increase with the bulk modulus of damper fluid, and the gap caused by bulk modulus expands with the increase of excitation frequency. The damping coefficients decrease with excitation frequency, and the

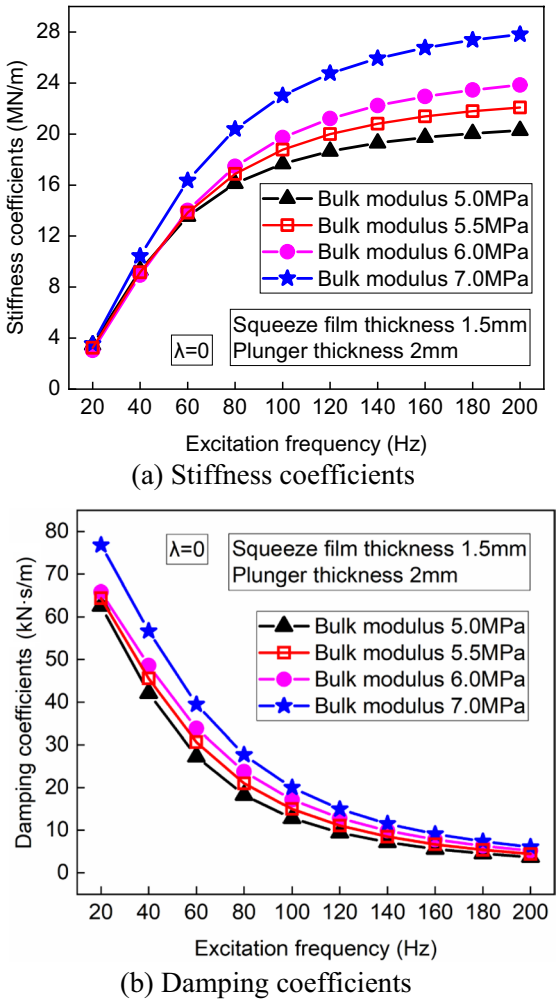


**Figure 8** Prediction of force coefficients for different bulk modulus of damper fluid

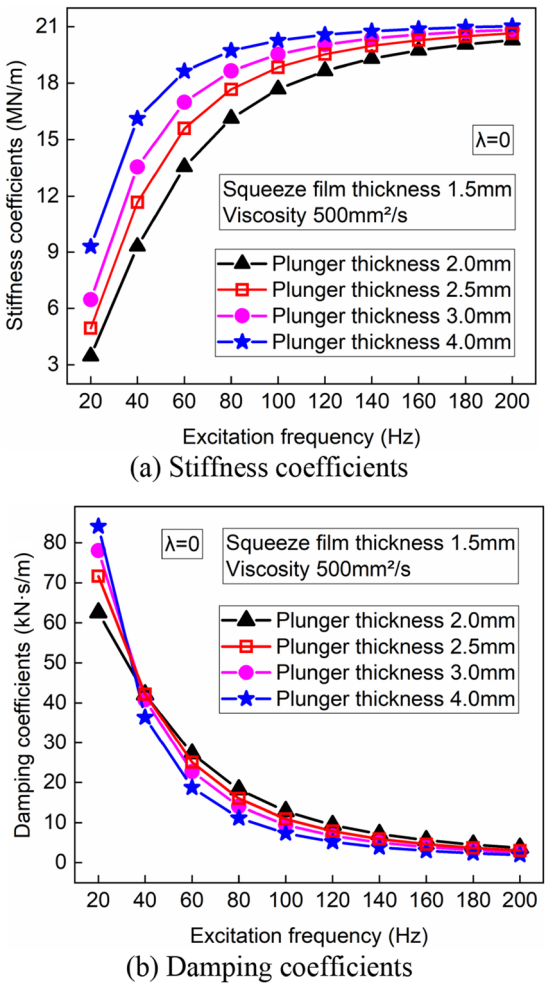


**Figure 9** Prediction of force coefficients for different thickness of plunger

deceleration rate of that keep decreases with frequency, as shown in Figure 8(b). The damping coefficients of HDSFD increases with bulk modulus at all the excitation frequency.

The predicted stiffness and damping coefficients of HDSFD versus different excitation frequencies and thickness of plunger is shown in Figure 9. As presented in Figure 9(a), the stiffness coefficients increase with the both excitation frequency and plunger thickness. The deviations of stiffness coefficients caused by plunger thickness decrease with excitation frequency. As shown in Figure 9(b), the damping coefficients decrease rapidly as the excitation frequency increases, and the larger the plunger thickness is, the faster the damping coefficient decreases. The maximum value of the predicted damping coefficients increases with the thickness of plunger. While the damping coefficient decreases with the increase of plunger thickness, when the excitation frequency is greater than 40 Hz.

Figure 10 shows the measured excitation force for three different structures of HDSFD. Figure 10(a) shows visually the excitation forces of the three types HDSFDs with time. It can be seen that the amplitude of the excitation force remains almost constant, which indicates that there is no significant nonlinear behavior of HDSFDs. For the same parameters, the excitation force of configuration-III is the largest, while the excitation force of configuration-I HDSFD is the smallest. Figure 10(b) shows the hysteresis curve of the three types HDSFDs. The hysteresis curves of the three types HDSFDs show a nearly perfect elliptical shape, which confirms again the linear character of the dampers. In addition, the slope of the line connecting the two farthest points of the hysteresis curve represents the stiffness factor. The area of the hysteresis curve

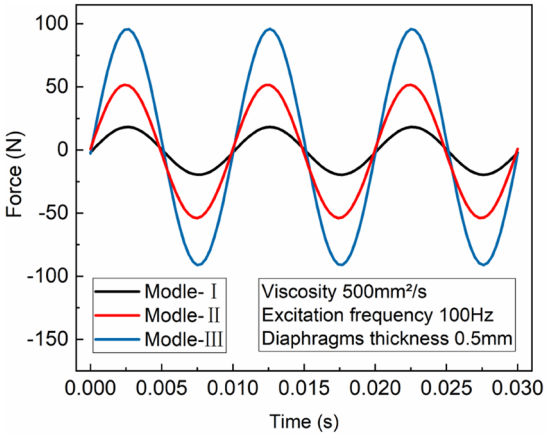


(a) Excitation force versus time

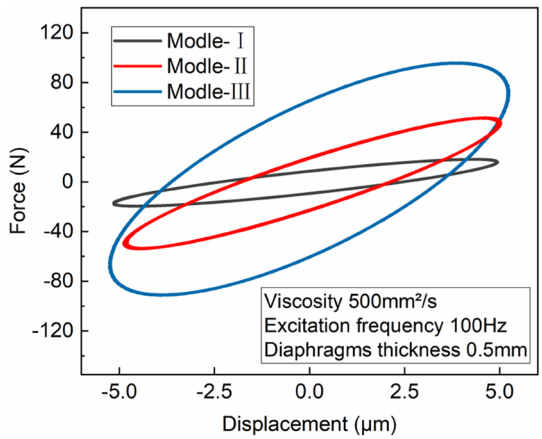


(b) Excitation force versus displacement

**Figure 10** Example experimental tests at 100Hz: Excitation force of the three types of HDSFDs

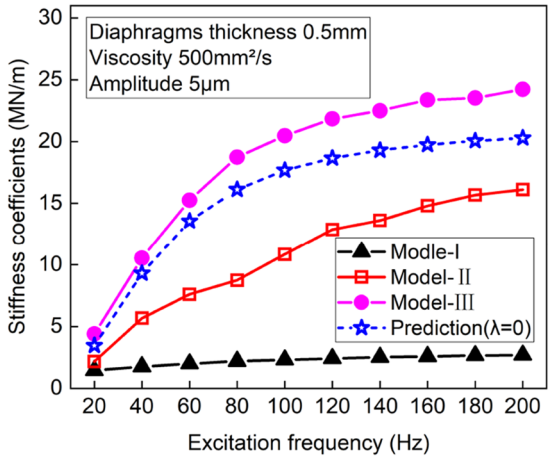


(a) Stiffness coefficients

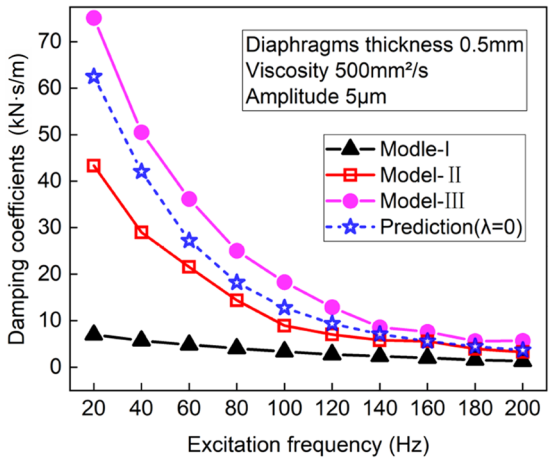


(b) Damping coefficients

**Figure 11** Force coefficients of HDSFDs versus excitation frequency with different structural

reflects the damping performance of the HDSFD to some extent.

Figure 11 shows the measured stiffness and damping coefficients with excitation frequency for three different structures of HDSFD. It can be seen from the figure that the stiffness coefficients of all of the three structures of HDSFD increase with excitation frequency, while the damping coefficients have the opposite trend. The stiffness and damping coefficients of configuration-I are significantly lower than those of configuration-II and configuration-III HDSFDs and configuration-III HDSFD presents the largest stiffness and damping coefficients. The force coefficients of configuration-II are increased by about four times compared to configuration-I, and the force coefficients of configuration-III are increased by half compared to configuration-II. The reason for the apparently small force coefficient of the configuration-I HDSFD is the weakening of the damper fluid film squeezing effect by the same directional motion of the diaphragm and the plunger, under the same conditions. The damping characteristics of configuration-III HDSFD are further improved by the presence of multiple damper fluid films in parallel and additional slit damping compared to configuration-II.

Figure 11 also includes the damping and stiffness predictions from the model mentioned above. The experimental force coefficients obtained from configuration-I and configuration-II are lower than the theoretical predictions, which can be attributed to the weakening of the damper fluid film squeeze effect by the flexibility of the diaphragm. The force coefficients obtained from configuration-III are larger than the theoretical predictions for almost all frequency, which can be attributed to the superimposed effect result from the compression of the damping film between the diaphragm and the modified pressure plate.

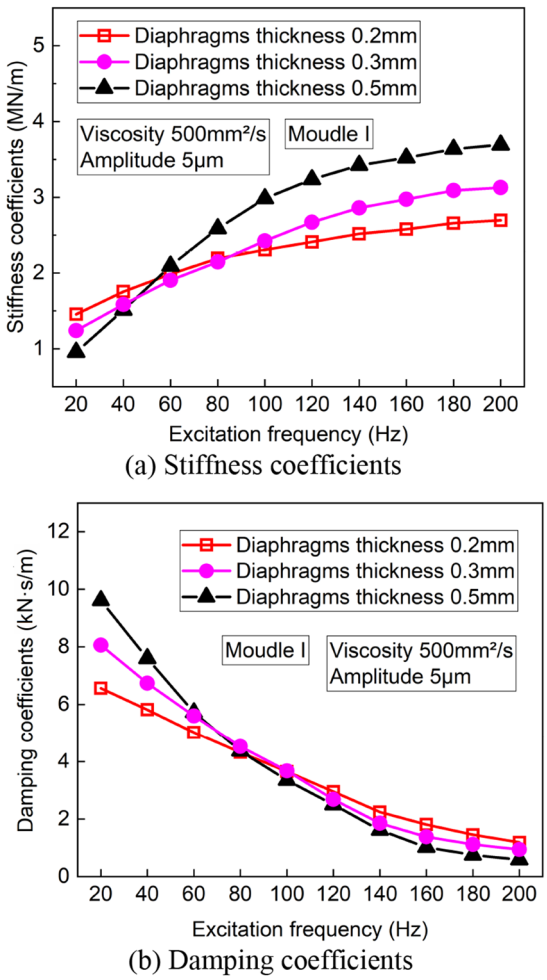


**Figure 12** Force coefficients of configuration-I HDSFD versus excitation frequency and diaphragms thickness

Figure 12 illustrates the measured stiffness and damping coefficients of configuration-I HDSFD versus excitation frequency and diaphragms thickness. It can be seen from Figure 12(a) that the stiffness coefficients of configuration-I HDSFD increase with excitation frequency. The growth rate of the stiffness coefficients increases with diaphragms thickness. The configuration-I with larger diaphragms thickness has a smaller minimum stiffness value and a higher peak stiffness value than those with smaller diaphragms. From Figure 12(b), It can be seen that the damping coefficients of configuration-I HDSFD decrease with excitation frequency. The rate of the stiffness coefficients decreases slow down with diaphragms thickness. The configuration-I with larger diaphragms thickness has a higher peak stiffness coefficient and a smaller minimum damping coefficient than those with smaller diaphragms.

This phenomenon can be attributed to the interaction between diaphragm deformation and damper fluid flow and its compression. Since configuration-I HDSFD with different thicknesses diaphragms have almost equal displacement induced volume change (DIVC) and different pressure induced volume change (PIVC), when the plunger is forced to vibrate [18]. Large diaphragm thickness of configuration-I HDSFD corresponds to a small PIVC, which leads to a large damping flow exchange between the different cavities. As the excitation frequency increases further (greater than 80 Hz), the damper fluid does not have enough time to flow and exchange between different cavities, which exhibits more pronounced compression behavior (and greater pressure difference between cavities) instead. Deformation of the diaphragms itself weakens the compression behavior of the damper fluid. Small diaphragm thickness leads to large PIVC and small damper fluid compression behavior, which ultimately causes small stiffness of configuration-I HDSFD at high frequencies. In addition, greater pressure difference between cavities means greater force on the plunger and more energy dissipation at the same displacement (amplitude). High energy dissipation in a given time (one excitation cycle) means high damping factor. Large pressure in the cavity causes significant compression of the damper fluid, which resulting in an increase in stiffness coefficients.

Figure 13 shows the measured excitation force of configuration-II HDSFD with diaphragm thickness. Figure 13(a) shows visually the excitation forces of configuration-II HDSFD versus time and diaphragm thickness. It can be seen that the amplitude of the excitation force does not vary with time, but increases with the increase of the diaphragm thickness. This can be attributed to the increase in the structural stiffness of the damper due to the increase in the diaphragm thickness. In addition, the increase in diaphragm thickness does not significantly affect the linear tensor of the damper. Figure 10(b) presents the hysteresis curve of configuration-II HDSFD. It can be seen that the greater the thickness of the diaphragm, the more pronounced the inclination of the hysteresis curve, which implies a greater stiffness factor. The envelope area of the hysteresis curve also increases with the increase of the thickness of the diaphragm.

Figure 14 shows the measured stiffness and damping coefficients of configuration-II HDSFD versus excitation frequency and diaphragms thickness. The stiffness coefficients of configuration-II HDSFD increase with excitation frequency, while the damping coefficients change opposite. Different from configuration-I HDSFD, both the stiffness and damping coefficients of configuration-II HDSFD keeps increasing with diaphragm thickness. This difference can be attributed to the hindering effect of the pressure plate on the elastic deformation of the diaphragms, which largely eliminates the effect of PIVC on

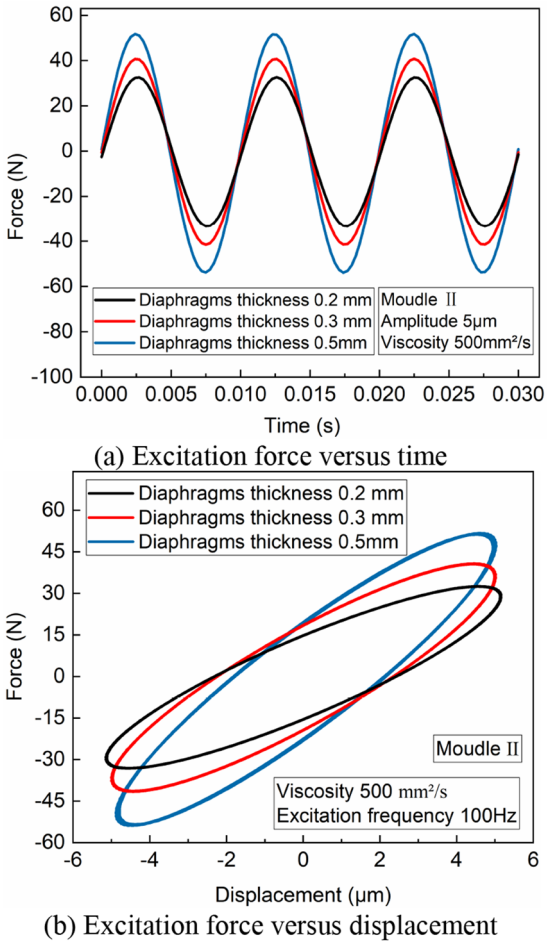


**Figure 13** Example experimental tests at 100 Hz: Excitation force of configuration-II HDSFD versus diaphragms thickness

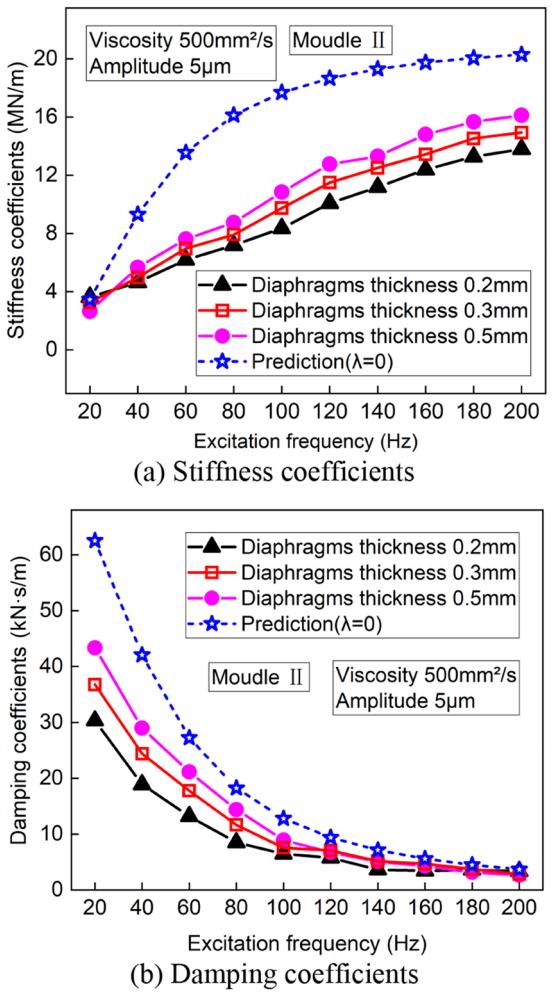


**Figure 14** Force coefficients of configuration-II HDSFD versus excitation frequency and diaphragms thickness

the force coefficient of configuration-II HDSFD. It should also be noted that the PIVC caused by the presence of the reserved hole at the center of pressure plate is not eliminated completely, resulting in differences both in stiffness and damping coefficients for configuration-II HDSFD with different diaphragm thicknesses at the same excitation frequency.

Figure 14 also includes the damping and stiffness predictions from the model mentioned above, which does not consider the effect of diaphragm flexibility. The experimental stiffness and damping coefficients obtained from configuration-II HDSFD are still lower than the theoretical predictions, but the discrepancy between the predictions and experiments gradually decreases with the increase of diaphragm thickness.

Figure 15 shows the stiffness and damping coefficients of configuration-II HDSFD as a function of excitation frequency and viscosity of damper fluid. Figure 15(a) shows that the stiffness coefficients increase as the viscosity of damper fluid increase. The minimum value of the stiffness coefficient of configuration-II HDSFD increases with the viscosity of the damper fluid. In addition, the discrepancy in stiffness coefficients for different viscosity damper fluid decreases with excitation frequency. Figure 15(b) shows that the damping coefficients of configuration-II HDSFD decrease with excitation frequency. The maximum damping coefficients of configuration-II HDSFD with a viscosity of 2000 $mm^2/s$ is bigger than that with a viscosity of 500 $mm^2/s$ and little than that with a viscosity of 1000 $mm^2/s$. In addition, the higher the viscosity of the damper fluid is, the faster the damping factor decreases with the excitation frequency. In other words, the greater of damper fluid viscosity is, the more significant the frequency dependence of configuration-II HDSFD for the same parameters. The damping coefficients decrease as the increase of damper fluid viscosity, when the excitation frequency is bigger than 40 Hz. The theoretical values of the stiffness and damping

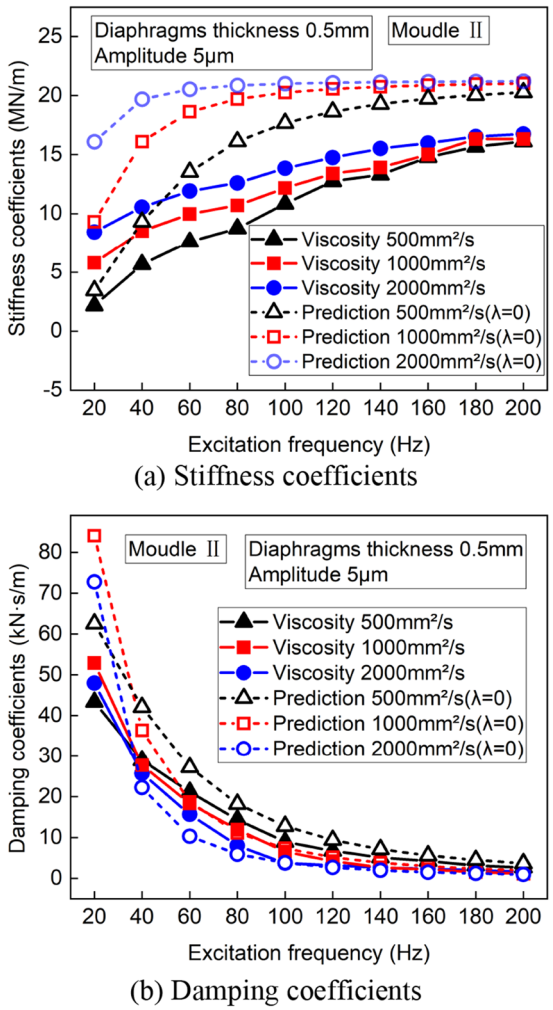


**Figure 15** Force coefficients of configuration-II HDSFD versus excitation frequency and viscosity of damper fluid

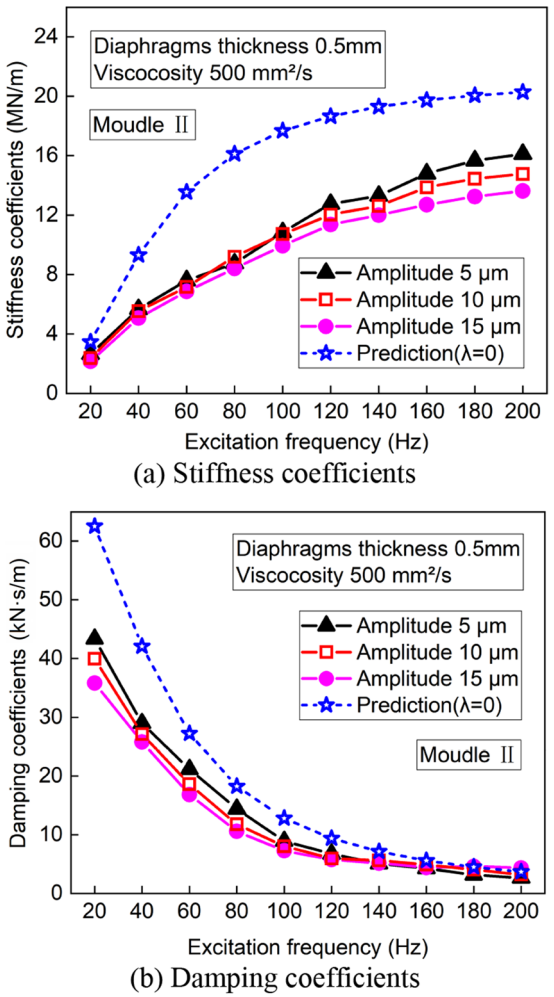


**Figure 16** Force coefficients of configuration-II HDSFD versus excitation frequency and amplitude

coefficients for the same conditions are also presented in Figure 15. The theoretical and experimental values share the same trend, and the difference between the theoretical and experimental values can be attributed to the elasticity of the diaphragms.

Figure 16 presents the force coefficients for the tests with three different amplitudes (5 μm, 10 μm and 15 μm) of configuration-II HDSFD versus excitation frequency. As presented in Figure 16(a), when the excitation frequency is low, the stiffness values corresponding to the three amplitudes are almost equal. As the excitation frequency increases further, the growth rate of stiffness decreases. At the same time, significant differences in the stiffness values corresponding to different amplitudes were observed. Figure 16(b) depicts the damping coefficients versus excitation frequency at different amplitudes. Contrary to the trend of the stiffness coefficients, the damping coefficients decreases rapidly with the increase of the excitation frequency, and then the rate of decrease tends to weaken. In addition, the discrepancy in damping coefficients with different amplitudes decrease with excitation frequency.

The theoretical values for the same conditions are also presented in Figure 16. Compared to the experimental value obtained with large amplitude, the experimental value obtained with a small amplitude is closer to the theoretical value. This can be attributed to the fact that the theoretical presented above ignores the effect of amplitude on the volume of the damper cavity. It is obvious that the smaller the amplitude, the smaller the effect on the volume of the damper cavity, and the closer the experimental value is to the predicted value.

Figure 17 shows the measured stiffness and damping coefficients of configuration-III HDSFD versus excitation frequency and diaphragms thickness. The stiffness

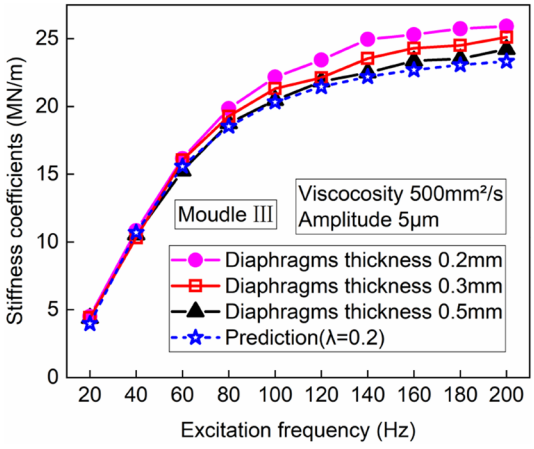


(a) Stiffness coefficients

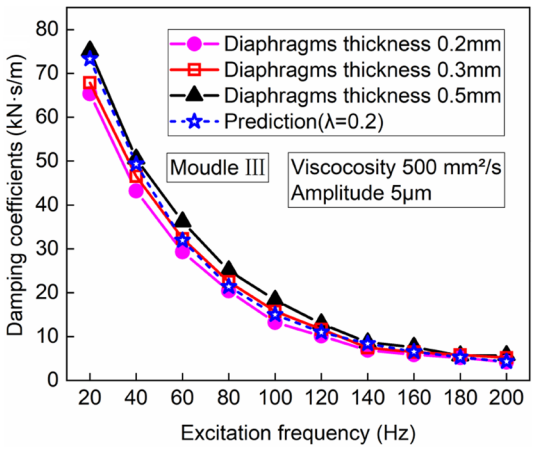


(b) Damping coefficients

**Figure 17** Force coefficients of configuration-III HDSFD versus excitation frequency and diaphragms thickness

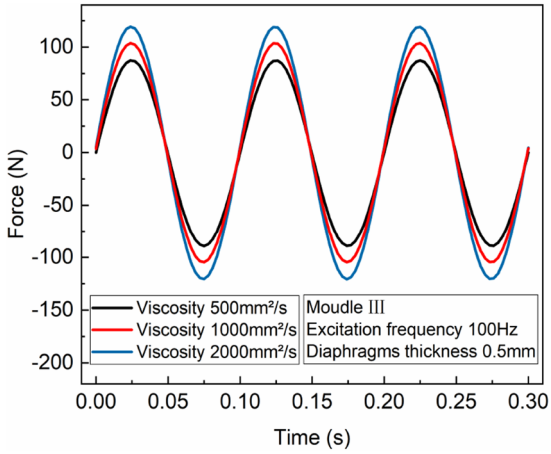


(a) Excitation force versus time

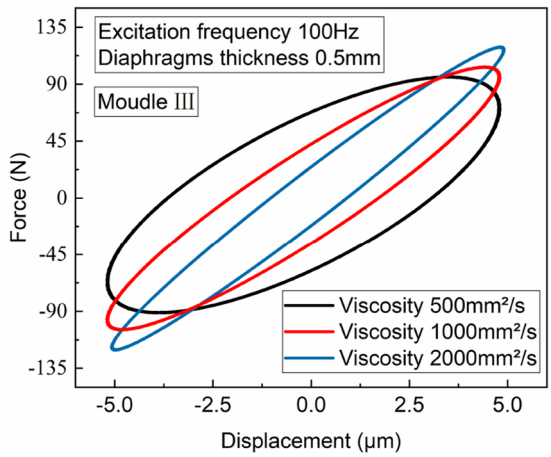


(b) Excitation force versus displacement

**Figure 18** Example experimental tests at 100 Hz: Excitation force of configuration-III HDSFD versus viscosity of the damper fluid

coefficients of configuration-III HDSFD increase with excitation frequency, while the damping coefficients change opposite. As can be seen from Figure 17(a) that the thickness of diaphragms has little effect on the stiffness coefficients when the excitation frequency is low (less than 60 Hz). When the excitation frequency is greater than 60 Hz, the stiffness coefficient of configuration-III HDSFD decreases with the increase of diaphragm thickness. From Figure 17(b), it can be seen that the damping coefficient increases with diaphragm thickness.

The difference in force coefficients between configuration-II and configuration-III HDSFD for the same parameters stems from the structural differences of them. The pressure plate (modified) mounted on configuration-III HDSFD do not obstruct the elastic deformation of the diaphragms. The large thickness of the diaphragm results in a similar DIVC and a small PIVC between diaphragms and pressure plate (modified), when the plunger is forced to vibrate, just like configuration-I HDSFD [20]. Large diaphragm thickness of configuration-III HDSFD corresponds to a small PIVC, which leads to a large damping flow exchange between the different cavities and a significant slit damping effect. Large diaphragm thickness causes significant compression of the damper fluid, which resulting in an increase in stiffness coefficients. Theoretical values for the same parameters are also presented in Figure 17. The predicted stiffness and damping coefficients show good agreement with the measured data.

Figure 18 presents an example experimental test at 100 Hz on the configuration-III HDSFD. Figure 18(a) shows visually the excitation forces versus time and viscosity of the damper fluid. It can be seen that the amplitude of the excitation force is not a function of time, but increases with viscosity of the damper fluid. Figure 18(b) presents the hysteresis curve of configuration-III HDSFD.

It can be seen that the viscosity of the damper fluid is positively correlated with the inclination of the hysteresis curve and negatively correlated with the area of the hysteresis curve envelope.

Figure 19 presents the stiffness and damping coefficients of configuration-III HDSFD as a function of excitation frequency and viscosity of the damper fluid. As presented in Figure 19(a), the stiffness coefficients of configuration-III increase with both excitation frequency and viscosity of the damper fluid. The minimum value of the stiffness coefficient of configuration-III HDSFD significantly improved with the damper fluid viscosity. In addition, the discrepancy in stiffness coefficients for different viscosity damper fluid decreases with the increase of excitation frequency. From Figure 19(b), it can be seen that the damping coefficients of configuration-III decrease with excitation frequency. Similar to the influences of viscosity on the damping coefficients of configuration-II, the damping coefficients of configuration-III do not increase with the viscosity of damper fluid consistently. The higher the viscosity of the damper fluid, the faster the damping coefficient decreases with the excitation frequency. The theoretical values for the same conditions are also presented in Figure 19. The predicted force coefficients of the MHDSFD shows good agreement with the experimental data, especially in the case of high excitation frequency.

Figure 20 presents an example experimental test at 100 Hz on the configuration-III HDSFD with different amplitude. Figure 20(a) shows visually the excitation forces versus time and amplitude. It can be seen that the amplitude of the excitation force increases with excitation amplitude. The excitation force acting on the configuration-III HDSFD at an amplitude of 15 μm is about twice as large as that at amplitude of 5 μm. Figure 20(b) presents the hysteresis curve of configuration-III HDSFD with different amplitude. It can be seen that the smaller the excitation amplitude, the more pronounced the slope

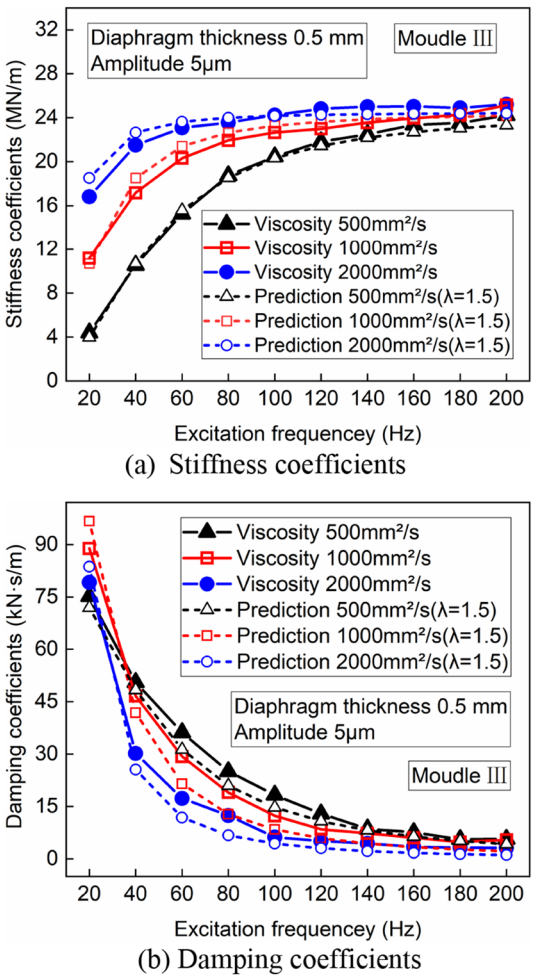


**Figure 19** Force coefficients of configuration-III HDSFD versus excitation frequency and viscosity of damper fluid

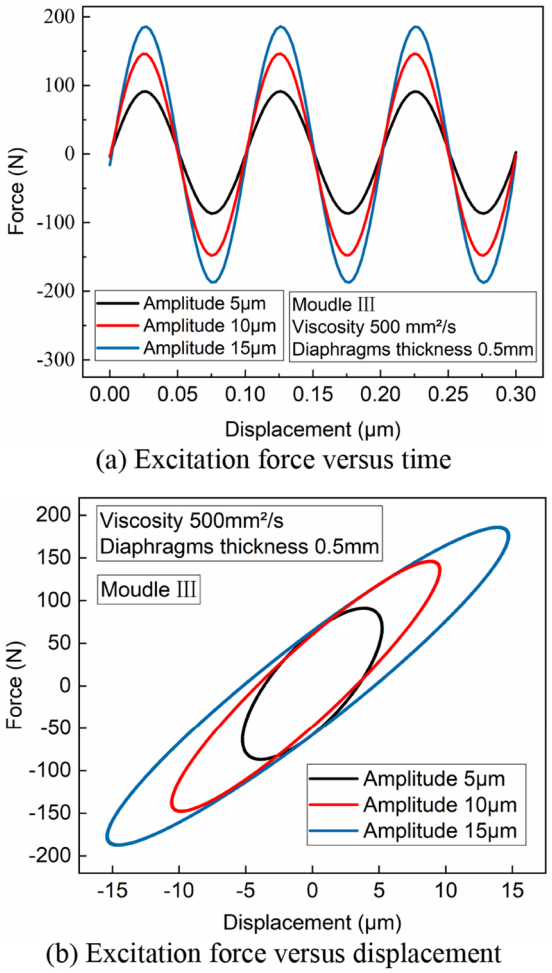


**Figure 20** Example experimental tests at 100 Hz: Excitation force of configuration-III HDSFD versus amplitude

of the hysteresis curve, which implies a greater stiffness factor. It should be emphasized that the increase in amplitude leads to a significant increase in the envelope area of the hysteresis curve, which does not imply a significant increase in the damping coefficients [21, 29].

Figure 21 shows the measured and predicted force coefficients of configuration-III HDSFD versus excitation frequency and excitation amplitude. The stiffness coefficients of configuration-III HDSFD increase with excitation frequency, and the discrepancy in stiffness coefficients with different amplitudes increase with excitation frequency. Contrary to the trend of the stiffness coefficients, the damping coefficients decrease with the excitation frequency. The discrepancy in damping coefficients with different amplitudes decrease with excitation frequency. In addition, the predicted stiffness and damping coefficients show good agreement with the measured data.

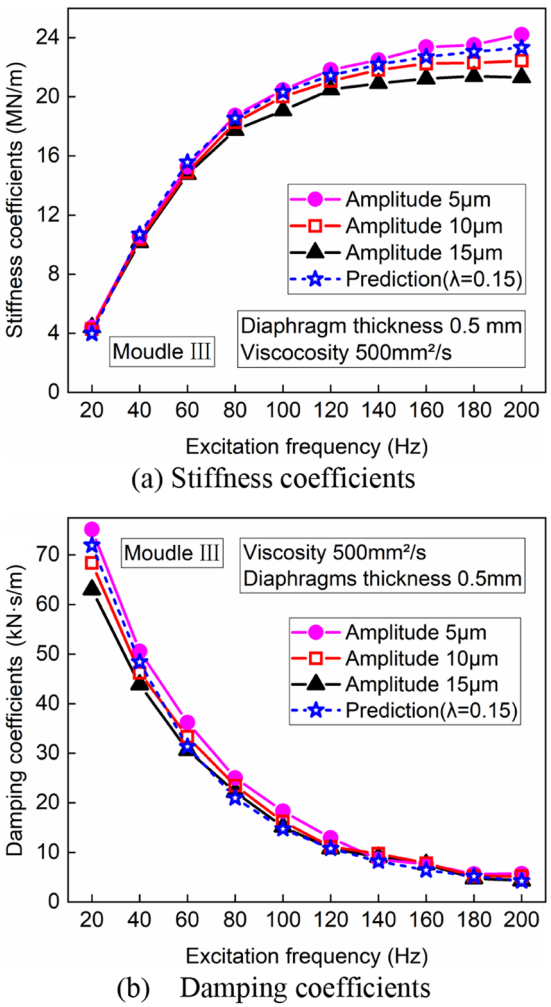


**Figure 21** Force coefficients of configuration-III HDSFD versus excitation frequency and amplitude

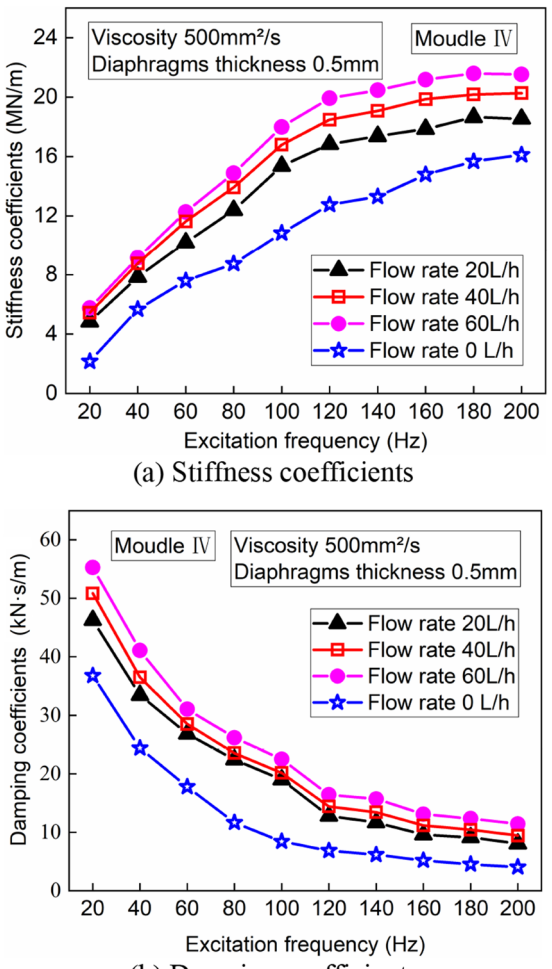


**Figure 22** Force coefficients of configuration-IV HDSFD versus excitation frequency and flow rate

Figure 22 shows the measured stiffness and damping coefficients of configuration-IV HDSFD versus excitation frequency and flow rate. It can be seen that the stiffness and damping coefficients of configuration-IV HDSFD increase with the increase of damper fluid supply flow rate, which can be attributed to the effect of external damper fluid supply on the pressure inside the damper cavity. The force coefficients from the test data without damper fluid supply case are also shown for reference. With the continuous supply of external damper fluid, the force coefficients of HDSFD still show a significant frequency-dependence. The damping coefficient at high frequency excitation with damper fluid supply is approximately twice as high as that without damper fluid supply.

## 6 Conclusions

The present work advanced a kind of DBSFD with a completely symmetrical structure, aimed for TPGBs system. Several HDSFDs structures with symmetrical structure were proposed for good damping performance. A dynamical model of HDSFD, which successfully presents the frequency dependence of force factors is presented. Based on the dynamic model, the effects of different parameters on the dynamic stiffness and damping of HDSFD are analyzed, and the results of the analysis serve as a guide for the determination of the structural parameters. An experimental test rig was built to test the performance of HDSFDs, and to verify the correctness of the dynamic model of HDSFD.

The damping levels generated with the HDSFDs (configuration-II and configuration-III HDSFD) are remarkable for TPGBs system. The stiffness and damping coefficients still show a significant frequency dependence, despite the highly symmetrical structure of HDSFDs. Another noteworthy conclusion is that multi-layer squeeze film structure can improve the damping performance of HDSFDs in the full frequency domain. In addition, using low viscosity damper fluid can improve damping characteristics in high frequency region to some extent. Finally, closed cycle supply of external damper fluid can significantly improve the damping performance of HDSFDs under high frequency excitation.

**Acknowledgements**
Not applicable.

**Authors' Contributions**
KF was in charge of the whole trial; JW wrote the manuscript; SH assisted with sampling and laboratory analyses. All authors read and approved the final manuscript.

**Funding**
Supported by National Key Research and Development Program of China (Grant No. 2021YFF0600208), National Natural Science Foundation of China (Grant No. 52005170), Hunan Provincial Science and Technology Innovation Program of China (Grant No. 2020RC4018).

**Data Availability**
All relevant data are within the paper. Data openly available in a public repository.

## Declarations

**Competing Interests**
The authors declare no competing financial interests.

Received: 28 October 2023 Revised: 22 March 2024 Accepted: 27 March 2024
Published online: 03 June 2024

**References**

[1] K Feng, J W Wang, H Li, et al. Theoretical and experimental investigation of porous tilting pad gas bearings with hermetic squeeze film dampers based on multilayer diaphragm structure. *Tribology Transactions*, 2023, 66(4): 746-759.
[2] S J Zhang, J J Yu, S To, et al. A theoretical and experimental study of spindle imbalance induced forced vibration and its effect on surface generation in diamond turning. *International Journal of Machine Tools and Manufacture,* 2018, 133: 61-71.
[3] L Andres, J Yang, R Mcgowan. Measurements of static and dynamic load performance of a 102 MM carbon-graphite porous surface tilting-pad gas journal bearing. *Journal of Engineering for Gas Turbines and Power*, 2021, 143(11): 111017.
[4] K Feng, Y Wu, W Liu, et al. Theoretical investigation on porous tilting pad bearings considering tilting pad motion and porous material restriction. *Precision Engineering*, 2018, 53: 26-37.
[5] S Li, Y Lu, Y Zhang, et al. Nonlinear dynamic response and bifurcation of asymmetric rotor system supported in axial-grooved gas-lubricated bearings. *Journal of Low Frequency Noise, Vibration and Active Control,* 2022, 41(2): 451-478.
[6] X Qin, X Wang, Z Qiu, Y Hao, et al. Experimental investigation for novel hybrid journal bearing with hydrostatic squeeze film and metal mesh damper in series. *Industrial Lubrication and Tribology*, 2023, 75(1): 1-8.
[7] C Zheng, J Wu, M Zhang, et al. Impact response and energy absorption of metallic buffer with entangled wire meshdamper. *Defence Technology*, 2023. https: //doi. org/10. 1016/j.dt.2023.12.008.
[8] B H Ertas, H Luo, D Hallman. Tuning the vibration of a rotor with shape memory alloy metalrubber supports. *Journal of Sound and Vibration,* 2015: 1-16.
[9] Y Lee, C Kim, T H Kim, et al. Effects of mesh density on static load performance of metal mesh gas foil bearings. *ASME. J. Eng. Gas Turbines Power,* 2012, 134(1): 012502. https:// doi.org/https://doi.org/10.1115/1.400 4142.
[10] K Feng, Y Liu, X Zhao, et al. Experimental evaluation of the structure characterization of a novel hybrid bump metal mesh foil bearing. *ASME J. Tribol*, 2016, 138(2): 021702.
[11] P Safarpour, H R Heidari. Design and modeling of a novel active squeeze film damper. *Mechanism and Machine Theory,* 2016, 105: 235-243.
[12] L Andres, S H Jeun. Squeeze film dampers: An experimental appraisal of their dynamic performance. *Asia Turbomachinery & Pump Symposium,* 2016: 22-25.
[13] Z Wang, Z Liu, G Zhang. Dynamic characteristics of elastic ring squeeze film damper. *Industrial Lubrication and Tribology*, 2019, 71(10): 1144-1151.
[14] E Gheller, S Chatterton, A Vania, et al. Squeeze film damper modeling: A comprehensive approach. *Machines*, 2022, 10(9): 781. https://doi.org/https://doi.org/10.3390/machines 1009 0781.
[15] V M Zaccardo, G D Buckner. Active magnetic dampers for controlling lateral rotor vibration in high-speed rotating shafts. *Mechanical Systems and Signal Processing*, 2021, 152: 107445.
[16] B H Ertas. Compliant hybrid journal bearings using integral wire mesh dampers. *Journal of Engineering for Gas Turbines and Power*, 2009, 131(2): 022503-022514.
[17] B H Ertas, A Delgad. Hermetically sealed squeeze film damper for operation in oil-free environments. *ASME J. Eng. Gas Turbines Power*, 2018, 141(2): 022503-022512.
[18] E Gheller, S Chatterton. A Vania, et al. Squeeze film damper modeling: A comprehensive approach. *Machines,* 2022, (10): 781-790.
[19] G Adiletta, Pietra, L Della. The squeeze film damper over four decades of investigations. Part ii: Rotordynamic analyses with rigid and flexible rotors. *Shock & Vibration Digest*, 2002, 34(2): 97-126.
[20] J W Wang, H Li, Y H Wu, et al. Performance analysis and test verification of porous tilting pad bearings with hermetically sealed squeeze film damper in parallel. *Journal of Mechanical Engineering*, 2023, 59(1): 151-161.
[21] K Gary, B H Ertas. Experimental rotordynamic force coefficients for a diffusion bonded compliant hybrid journal gas bearing utilizing fluid-filled hermetic dampers. *Journal of Engineering for Gas Turbines and Power*, 2020, 142(4): 041008-041015.

[22] G Huang, X Wang, X Qin, et al. Experimental investigation of dynamic behavior of rotor system with a novel double layers flexible support tilting pad bearing. *Advances in Mechanical Engineering,* 2022, 14(8): 6482.
[23] A Delgado, B H Ertas. Dynamic characterization of a novel externally pressurized compliantly damped gas-lubricated bearing with hermetically sealed squeeze film damper modules. *ASME. J. Eng. Gas Turbines Power,* 2019, 141(2): 021028-021037.
[24] B H Ertas, K Gary. Frequency dependancy of dynamic force coefficients for hermetic squeeze film dampers utilizing fluid-bounding flexible structures. *Journal of Engineering for Gas Turbines and Power: Transactions of the ASME,* 2020, (4): 142-156.
[25] X Lu, L Andrés, B Koo, et al. On the effect of the gap of end seals on force coefficients of a test integral squeeze film damper: Experiments and predictions. *ASME. J. Eng. Gas Turbines Power*, 2021, 143(1): 011014-011028.
[26] K Li, X Yin, Z Zong, et al. Estimation of porosity, fluid bulk modulus, and stiff-pore volume fraction using a multitrace bayesian amplitude variation with offset petrophysics inversion in multi porosity reservoirs. *Journal of the Society of Exploration Geophysicists*, 2022, 87(4): 1-11.
[27] M Kamel, K Mohammadifard. Comparison of bulk modulus as benzene dense fluid using the lir equation of state with the extended coefficients and comparison with peng-robinson equation of state. *Journal of Chemistry Letters*, 2020, 1(3): 103-110.
[28] X Jiao, Y Zhao, W Ma. Nonlinear dynamic characteristics of a micro-vibration fluid viscous damper. *Nonlinear Dynamics*, 2018, 92: 1167-1184.
[29] X Jiao, Y Zhao, W Ma. Normalized study of three parameter system in the time domain and frequency domain. *Shock and Vibration,* 2017: 1-21.

**Jianwei Wang,** born in 1990, is currently a Ph.D. candidate at *Hunan University, China*.

**Haoxi Zhang,** born in 1991, is currently a Ph.D. candidate at *Hunan University, China*.

**Shaocun Han,** born in 1997, is currently a Ph.D. candidate at *Hunan University, China*.

**Hang Li,** born in 1998, received his master degree in mechatronics from *Hunan University, China*, in 2022.

**Peng Wang,** born in 1994, received his Ph.D. degree in mechatronics from *Hunan University, China*, in 2023.

**Kai Feng,** born in 1988, is a professor at *Hunan University, China*.